Asian Journal of Chemistry; Vol. 38, No. 11 (2026), 2975-2986
ASIAN JOURNAL OF CHEMISTRY
https://doi.org/10.14233/ajchem.2026.36827

Graphene Oxide-Metal Oxide Nanocomposites for Solar Photocatalytic Dye Degradation: A Comparative Study of GO/ZnO and GO/TiO_2

ASHISH SHARMA, ANIL YADAV*, and BRIJNANDAN S. DEHIYA

Department of Chemical Engineering, Deenbandhu Chhotu Ram University of Science and Technology, Murthal-131039, India

*Corresponding author: E-mail: anilyadav.che@dcrustm.org

Received: 14 July 2026 *Accepted*: 7 October 2026 *Published online*: 13 November 2026 AJC-22528

The present study focuses on the synthesis of graphene oxide (GO), ZnO, TiO_2 and GO-based metal oxide nanocomposites (GO/ZnO and GO/TiO_2) *via* a chemical method. The samples prepared were characterized using various techniques such as XRD, FTIR, HRTEM and SEM to analyze their structural, morphological and functional properties. The photocatalytic activity of the synthesized materials was evaluated by studying the degradation of Rose Bengal and methylene blue dyes in aqueous solutions under natural sunlight. The results proved that the GO-based nanocomposites degraded both dyes faster than the ZnO and TiO_2 samples. Among the prepared nanocomposites, GO/ZnO (1:7) showed the fastest degradation, with a comparable final removal of the dyes; these results indicate that GO-supported metal oxide nanocomposites can be used as sunlight-responsive photocatalysts for the degradation of dyes in contaminated water.

Keywords: Graphene oxide, ZnO, TiO_2, GO-based nanocomposites, Photocatalysis, Dye degradation.

INTRODUCTION

Water pollution is a major environmental problem in the 21st century and affects water quality, human health and ecosystem stability across the world [1]. Only about 2.5% of the total water on earth is freshwater and these resources are increasingly affected by human activities such as industrialization, urbanization, mining and agriculture [2,3]. The untreated discharge of industrial effluents is a major contributor to aquatic pollution. Dyes released from textile manufacturing and other sectors such as food processing and pharmaceutical and cosmetic production are a significant concern. Their complex aromatic structures often resist conventional wastewater treatment processes. Even small amounts can alter water quality through persistent colouration. Some dye breakdown products may pose additional risks to aquatic life and human health [1,4-6].

Photocatalytic treatment has gained attention as a method for removing organic contaminants from wastewater. It relies on light-driven reactions to break down harmful compounds and can minimize the need for additional chemical treatment agents [1,7,8]. Titanium dioxide (TiO_2) and zinc oxide (ZnO) are widely investigated as semiconductor photocatalysts due to their chemical stability and relatively low toxicity [9]. Upon light exposure, these materials generate electron–hole pairs. The resulting charge carriers interact with water and dissolved oxygen to form reactive species that attack organic pollutants [7,8]. Their practical efficiency is limited by rapid electron–hole recombination and low quantum efficiency. Their wide band gaps of approximately 3.2 eV restrict light absorption mainly to the ultraviolet region. A gradual loss of photocatalytic activity can further affect their performance during treatment [1,8,10].

Graphene oxide (GO), commonly known as graphitic oxide, has attracted interest as a graphene precursor and as a functional support for photocatalytic materials [11,12]. The oxidation of graphite was first described by Brodie and later modified by Staudenmaier. The Hummers' method introduced in 1958 remains a widely used route for GO preparation [11-14]. Its structure contains hydroxyl, epoxy, carbonyl and carboxyl groups [15,16]. These oxygen containing functionalities improve water dispersibility and provide active sites for adsorption. They increase the interlayer spacing and facilitate the exfoliation of graphite oxide into individual sheets. The coexistence of sp^2- and sp^3-hybridized carbon domains further provides sites for interaction with other materials [15,16].

This is an open access journal, and articles are distributed under the terms of the Attribution 4.0 International (CC BY 4.0) License. This license lets others distribute, remix, tweak, and build upon your work, even commercially, as long as they credit the author for the original creation. You must give appropriate credit, provide a link to the license, and indicate if changes were made.

Integration of GO with semiconductor oxides such as ZnO and TiO_2 offers a route to hybrid photocatalysts with modified charge-transfer and surface properties. GO can accept and transport photogenerated electrons. This may suppress electron-hole recombination and improve pollutant adsorption [15-17]. Its sheet-like structure can limit nanoparticle aggregation and help retain metal oxide particles within the composite. Such features may improve catalyst recovery and reduce particle release into treated water [16]. However, the influence of GO loading on degradation efficiency and reaction kinetics under natural sunlight also requires further investigation. A systematic comparison of GO/ZnO and GO/TiO_2 composites with different composition ratios can help establish the role of GO content in photocatalytic performance.

The present study examines GO/ZnO and GO/TiO_2 nanocomposites with GO-to-metal oxide ratios of 1:9 and 1:7 for the degradation of methylene blue and Rose Bengal dyes under natural sunlight. The photocatalytic efficiency and degradation kinetics of the different compositions were compared. GO/ZnO (1:7) exhibited the highest activity with faster degradation kinetics under the tested conditions. The work evaluates the potential of GO-supported ZnO and TiO_2 composites for sunlight-driven dye removal from aqueous solutions.

EXPERIMENTAL

The chemicals used in this study included graphite (SRL), sulphuric acid (HiMedia), potassium permanganate (SRL) and hydrogen peroxide (HiMedia) for the synthesis of graphene oxide (GO). Zinc acetate (Fisher Scientific), sodium hydroxide (Emplura), titanium isopropoxide (SRL), ethylene glycol (Qualigens) and distilled water were used for the preparation of ZnO and TiO_2 nanoparticles through hydrothermal and sol–gel methods.

Characterization: The experimental procedures were carried out using a magnetic stirrer (Labquest Borosil), hot air oven (Biogenix), ultrasonic cleaner (UM-2022-6L, Jupiter Engineering Works, India), centrifuge (Remi R-8C Plus), agate mortar and pestle, muffle furnace (K1-180, Khera Instruments, India) and hydrothermal autoclave. The structural and morphological characterization was performed using X-ray diffraction (Bruker), Fourier-transform infrared spectroscopy (FTIR, Perkin-Elmer Frontier), scanning electron microscopy (SEM, JEOL JSM-6100) and high-resolution transmission electron microscopy (HRTEM, JEOL JEM-2100 Plus). Photocatalytic degradation was monitored using a UV-Vis spectrophotometer (Rigol™).

General procedure

Synthesis of ZnO NPs by hydrothermal method: ZnO NPs were synthesized *via* a hydrothermal route using zinc acetate dihydrate $Zn(CH_3COO)_2{\cdot}2H_2O$ and sodium hydroxide (NaOH) as precursors. A zinc acetate solution was prepared in distilled water and stirred at 300 rpm for 30 min. Subsequently, NaOH solution was added slowly drop by drop under stirring until the pH reached 9. The resulting homogeneous mixture was transferred to a Teflon-lined stainless-steel autoclave and heated at 150 ºC for 8 h under sealed conditions. After natural cooling to room temperature, the obtained white precipitate was collected, washed thoroughly with distilled water and filtered. The product was then annealed at 500 ºC for 3 h in a muffle furnace to obtain crystalline ZnO NPs. Temperature and pH were observed during the synthesis. All experiments were carried out in triplicate to check the reproducibility of the results.

Synthesis of TiO_2 NPs by sol-gel method: TiO_2 NPs were prepared by the sol-gel method using titanium isopropoxide as the precursor. Titanium isopropoxide was mixed with ethylene glycol in a 1:3 ratio under continuous stirring. The resulting solution was heated on a hot plate at 130 ºC for 8 h to facilitate gel formation. The pH of the obtained solution was observed before thermal treatment. The resulting material was then annealed at 600 ºC for 3 h in a muffle furnace and allowed to cool naturally to room temperature. The obtained white TiO_2 nano-powder was collected and used for further characterization.

Synthesis of graphene oxide: Graphene oxide (GO) was prepared using a modified Hummers' method. In brief, 1 g of graphite powder was added in 23 mL of conc. H_2SO_4 under continuous magnetic stirring. Then, $KMnO_4$ (3 g) was added slowly while keeping the reaction temperature below 5 ºC using an ice bath to control the heat produced during oxidation. After the addition of $KMnO_4$, the reaction mixture was allowed to reach room temperature and stirred for 2 h. Distilled water was added slowly followed by the dropwise addition of 5 mL of H_2O_2 until a yellowish-brown colour developed, which established the successful oxidation of graphite. The resulting product was repeatedly washed and centrifuged (4000 rpm, 10 min per cycle) until neutral pH was attained. The suspension was then filtered and dried in a hot-air oven at 80 ºC for 24 h to obtain graphene oxide powder.

Synthesis of GO/ZnO nanocomposite (1:9 and 1:7) by hydrothermal method: The GO/ZnO nanocomposites were prepared by dispersing GO in deionized water through ultrasonication. Pre-synthesized ZnO NPs were then added to the GO suspension at GO mass ratios of 1:9 (50 mg:450 mg) and 1:7 (50 mg:350 mg) followed by ultrasonication for 30 min to ensure homogeneous dispersion. The mixture was transferred into a Teflon-lined autoclave and hydrothermally treated at 120 ºC for 12 h. The resulting suspension was centrifuged at 4000 rpm for 10 min and then dried at 100 ºC for 4 h to obtain the GO/ZnO nanocomposites.

Synthesis of GO/TiO_2 nanocomposite (1:9 and 1:7) by hydrothermal method: The GO/TiO_2 nanocomposites were synthesized using a similar hydrothermal procedure. GO was then dispersed in deionized water by ultrasonication, followed by the addition of pre-synthesized TiO_2 NPs at GO mass ratios of 1:9 (50 mg:450 mg) and 1:7 (50 mg:350 mg). After ultrasonication for 30 min, the suspension was transferred to a Teflon-lined autoclave and heated at 120 ºC for 12 h. The obtained product was centrifuged at 4000 rpm for 10 min and then dried at 100 ºC for 4 h to yield the GO/TiO_2 nanocomposites.

Photocatalytic activity: The photocatalytic performance of GO, GO/ZnO and GO/TiO_2 was evaluated through the degradation of methylene blue (MB) and rose Bengal (RB) dyes under natural sunlight. Experiments were conducted from 1 June to 31 July under clear-sky conditions between 11:00

AM and 2:00 PM at DCRUST, Murthal, India (coordinates 29.0251ºN, 77.0579ºE), at an average ambient temperature of 34 ± 2 ºC. Experiments were conducted only on days when no visible cloud cover was observed during the irradiation period. The photocatalytic experiments were conducted on different days since the pristine materials and GO-based nanocomposites were synthesised sequentially. Variations in the natural sunlight between experimental days may have influenced the observed degradation rates and represent a limitation of this study.

A catalyst dosage of 0.010 g (0.10 g L^{-1}) was maintained in 100 mL of 25 ppm dye solution for all experiments. The suspensions were stirred in the dark for 30 min to establish adsorption–desorption equilibrium. The dye concentration measured at the end of this period was taken as C_o for the subsequent sunlight exposure. Any decrease in dye concentration during dark stirring was attributed to adsorption and excluded from the sunlight-driven decolorization analysis. The suspensions were then exposed to natural sunlight under continuous stirring at 500 rpm. Aliquots of 5 mL were withdrawn at fixed time intervals and analysed using a UV-Vis spectrophotometer over the 200-800 nm range. Dye removal was monitored by recording the decrease in absorbance at 664 nm for methylene blue (MB) and 550 nm for rose Bengal (RB). In this study, degradation refers to dye decolourization based on the reduction in absorbance at the characteristic wavelength of each dye.

The photocatalytic degradation efficiency was calculated using the eqn. 1:

$$\text{Degradation efficiency (\%)} = \frac{C_o - C}{C_o} \times 100 \qquad (1)$$

where C_o is the dye concentration measured after 30 min of dark stirring, immediately before the start of sunlight irradiation and C is the dye concentration at irradiation time t.

The apparent reaction rate constant (k_{app}) was determined using the pseudo-first-order kinetic model using eqn. 2:

$$\ln\left(\frac{C_o}{C}\right) = k_{app} t \qquad (2)$$

where k_{app} is the apparent reaction rate constant, t is the irradiation time; C_o is the dye concentration immediately before sunlight irradiation; and C is the dye concentration at irradiation time t. A larger k_{app} value indicates faster apparent degradation kinetics under the investigated conditions.

RESULTS AND DISCUSSION

XRD analysis: Fig. 1 presents the XRD patterns of the pristine materials and synthesized nanocomposites. XRD analysis was performed to identify the crystalline phases and assess the structural characteristics of the prepared materials. ZnO exhibited characteristic reflections at 2θ = 31.61º, 34.31º and 36.08º. These peaks correspond to the (100), (002) and (101) planes of hexagonal wurtzite ZnO (JCPDS No. 36-1451). The average crystallite size was 27.41 nm with lattice parameters of a = 3.27 Å and c = 5.238 Å. These values are consistent with reported data [18,19]. TiO_2 displayed diffraction peaks at 25.3º, 27.5º, 36.0º, 41.3º, 54.4º and 56.6º. These reflections correspond to the anatase (101) and rutile (110), (101), (111), (211) and (220) planes. The diffraction pattern confirms a mixed anatase-rutile phase with anatase as the predominant structure. The average crystallite size was approximately 15 nm [20-23].

GO showed a prominent (001) reflection at 10.9º and a weak (100) reflection at 42.32º (JCPDS No. 23-64). The disappearance of the graphite peak near 26º supports the conversion of graphite into GO through oxidation. The calculated crystallite size and interlayer spacing were 12.8 nm and 0.81 nm, respectively [24,25]. The GO/ZnO (1:9) nanocomposite retained the characteristic ZnO reflections at 31.78º, 34.46º, 36.25º, 47.51º and 56.58º. These peaks were indexed to the (100), (002), (101), (102) and (110) planes. A weak GO (001) reflection appeared at 12.19º. The pattern confirms the presence of both crystalline ZnO and GO without detectable additional crystalline impurity phases. The average crystallite size was approximately 30 nm [26-29]. GO/TiO_2 (1:9) exhibited characteristic anatase reflections at 25.27º, 37.02º, 48.10º, 53.92º and 55.15º. These peaks correspond to the (101), (004), (200), (105) and (211) planes. A weak GO reflection was also observed. The average crystallite size was 23 nm [30-32].

The GO/ZnO (1:7) nanocomposite displayed a weak GO (001) reflection at 10.61º along with ZnO peaks at 31.74º, 34.50º, 36.31º, 47.50º, 56.59º, 62.87º, 66.44º, 68.10º, 69.85º, 72.62º, 76.90º and 81.42º. These reflections were indexed to the (100), (002), (101), (102), (110), (103), (200), (112), (201), (004), (202) and (104) planes of hexagonal wurtzite ZnO. No additional crystalline phases were detected. The average crystallite size was 20.38 nm [28,33]. GO/TiO_2 (1:7) exhibited a weak GO reflection at 10.41º and anatase TiO_2 peaks at 25.24º, 37.83º, 47.96º, 53.89º, 55.08º, 62.65º, 68.87º, 70.30º and 75.05º. These peaks correspond to the (101), (004), (200), (105), (211), (204), (116), (220) and (215) planes. The average crystallite size was approximately 10.1 nm. The diffraction pattern confirms the coexistence of GO and anatase TiO_2 without detectable additional crystalline impurity phases [34].

FTIR analysis: The FTIR spectra displayed characteristic vibrational bands of ZnO, TiO_2, GO and their nanocomposites. ZnO showed a broad O–H stretching band at 3428.58 cm^{-1} due to surface hydroxyl groups and adsorbed water. Weak C–H stretching was observed at 2929.68 cm^{-1} (Fig. 2). The bands at 1420.11 and 1135.23 cm^{-1} were assigned to hydroxyl bending/surface carbonate and C–O vibrations, respectively. The band at 902.41 cm^{-1} was attributed to Zn–OH vibrations. A characteristic Zn–O stretching band appeared at 425.80 cm^{-1} [35]. TiO_2 exhibited broad O–H stretching bands across 3700-3200 cm^{-1} and an H–O–H bending band at 1623.24 cm^{-1}. A weak atmospheric CO_2 band appeared at 2343.77 cm^{-1}. The Ti–O–Ti stretching vibration was observed at 676.24 cm^{-1} [32].

GO displayed characteristic bands of oxygen containing functional groups. These included O–H stretching at 3408 cm^{-1} and C–H stretching at 2974 cm^{-1}. The C=O stretching band appeared at 1728 cm^{-1}. The band at 1627 cm^{-1} corresponded to the sp^2 C=C skeletal vibration. C–OH bending and epoxy C–O–C stretching bands were observed at 1368 and 1213 cm^{-1}, respectively. These features support the oxidation of graphite to GO [36-40].

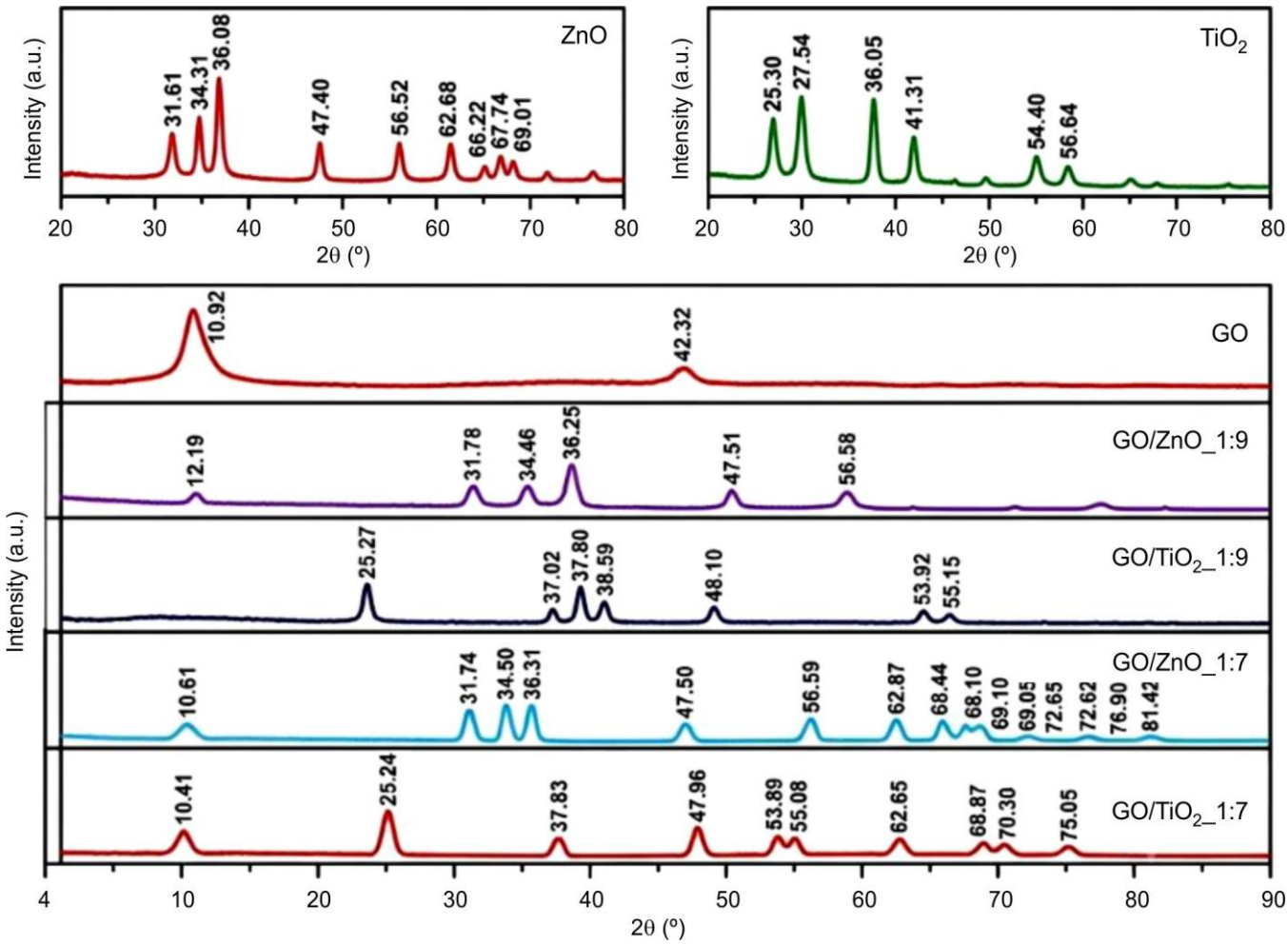


Fig. 1. XRD patterns of ZnO, TiO_2, GO, GO/ZnO (1:9), GO/TiO_2 (1:9) GO/ZnO (1:7), GO/TiO_2 (1:7)

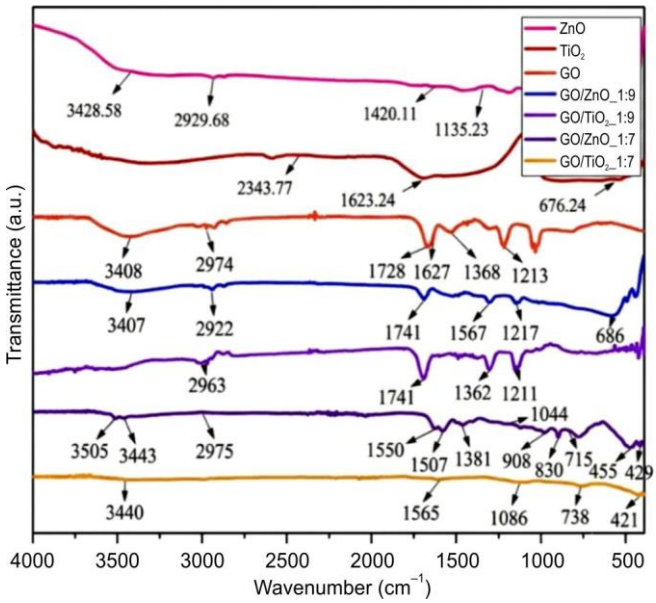


Fig. 2. FTIR spectra of ZnO, TiO_2, GO, GO/ZnO (1:9), GO/TiO_2 (1:9) GO/ZnO (1:7), GO/TiO_2 (1:7)

The GO/ZnO (1:9) nanocomposite exhibited O–H stretching at 3407 cm^{-1} and C–H stretching at 2922 cm^{-1}. Other bands appeared at 1741 cm^{-1} (C=O), 1581 cm^{-1} (sp^2 C=C), 1367 cm^{-1} (C–OH), 1217 cm^{-1} (epoxy C–O–C) and 686 cm^{-1} (Zn–O). Compared with bare GO, the C=O band shifted from 1728 to 1741 cm^{-1} while the sp^2 C=C band shifted from 1627 to 1581 cm^{-1}. These shifts indicate changes in the chemical environment of the GO functional groups following ZnO incorporation [16,41-43]. GO/TiO_2 (1:9) showed GO-related bands at 2963, 1741, 1362 and 1211 cm^{-1} along with Ti–O–Ti lattice vibrations below 700 cm^{-1}. The C=O band shifted from 1728 to 1741 cm^{-1} compared with bare GO. This shift suggests a change in the chemical environment of the carbonyl groups following TiO_2 incorporation [31,32,44,45].

The GO/ZnO (1:7) nanocomposite displayed broad O–H stretching bands at 3505 and 3443 cm^{-1} and C–H stretching at 2975 cm^{-1}. The sp^2 C=C vibrations appeared at 1550 and 1507 cm^{-1}. Other bands were assigned to O–H bending/C–OH stretching at 1381 cm^{-1} and C–O vibrations at 1044 cm^{-1}. The bands at 908, 830 and 715 cm^{-1} were attributed to C–O–C and aromatic C–H vibrations. Zn–O stretching bands appeared at 455 and 429 cm^{-1}. The sp^2 C=C bands shifted from 1627 cm^{-1} in bare GO to 1550 and 1507 cm^{-1} in the composite. The C–OH band also shifted from 1368 to 1381 cm^{-1}. These changes point to alterations in the chemical environment of the GO functional groups after ZnO incorporation. GO/TiO_2

(1:7) exhibited O–H stretching at 3440 cm^{-1} and C–H stretching at 2960 cm^{-1}. The sp^2 C=C and C–O stretching bands appeared at 1565 and 1086 cm^{-1}, respectively. Ti–O–Ti and Ti–O lattice vibrations were observed at 738 and 421 cm^{-1}. The shift of the sp^2 C=C band from 1627 to 1565 cm^{-1} further supports a change in the chemical environment of GO following TiO_2 incorporation.

Scanning electron microscopy (SEM): The SEM micrographs of GO, ZnO, TiO_2 and their nanocomposites, recorded at ×350 magnification and an accelerating voltage of 15 kV, revealed distinct morphological characteristics (Fig. 3). GO (Fig. 3a) displayed crumpled and loosely stacked sheet-like structures characteristic of graphene oxide. ZnO nanoparticles (Fig. 3b) exhibited aggregated granular and rod-like features. TiO_2 (Fig. 3c) showed densely packed fine particles with noticeable agglomeration. In the GO/ZnO (1:9) composite (Fig. 3d), ZnO nanoparticles were distributed across the GO sheets with moderate aggregation. GO/TiO_2 (1:9) (Fig. 3e) showed clustered TiO_2 nanoparticles deposited on the GO layers. The GO/ZnO (1:7) composite (Fig. 3f) exhibited larger agglomerated clusters at higher GO content. GO/TiO_2 (1:7) (Fig. 3g) displayed TiO_2 nanoparticles distributed across the GO sheets with a rough and heterogeneous surface. The SEM images reveal variations in surface morphology and nanoparticle distribution among the composites. The increased surface roughness may influence their photocatalytic behaviour [46].

HRTEM: GO (Fig. 4a) exhibited thin, transparent, wrinkled nanosheets with folded and overlapping regions, characteristics of the sheet-like morphology of graphene oxide. The crumpled morphology and irregular edges are consistent with structural defects and oxygen containing functional groups introduced during oxidation process. ZnO nanoparticles (Fig. 4b) displayed predominantly spherical morphology with slight agglomeration and an average particle size of approximately 45 nm and well-defined particle boundaries. TiO_2 nanoparticles (Fig. 4c) exhibited nearly spherical particles with relatively uniformly distribution and an average particle size of approximately ~35 nm, with a comparatively narrow particle-size distribution. In the GO/ZnO (1:9) nanocomposite (Fig. 4d), densely packed ZnO NPs (~40 nm) were observed on the GO nanosheets with partial agglomeration, which resulted in the close physical while partially obscuring the underlying GO sheets. In contrast, GO/TiO_2 (1:9) (Fig. 4e) showed relatively well-dispersed spherical TiO_2 NPs (~33 nm) distributed over clearly visible GO sheets with reduced agglomeration. The GO/ZnO (1:7) nanocomposite (Fig. 4f) showed more clearly visible GO sheets, with moderately dispersed ZnO NPs of ~32 nm and reduced clustering compared to the 1:9 composition. Similarly, GO/TiO_2 (1:7) (Fig. 4g) revealed relatively well-dispersed TiO_2 NPs with minimal aggregation and an average particle size of ~26 nm, with transparent GO sheets visible around the nanoparticles. Based on the HRTEM images, ZnO and TiO_2 NPs were observed in close physical contact with the GO sheets. Compared with the 1:9 compositions, the 1:7 nanocomposites showed finer particle dispersion and fewer agglomerated regions. This resulted in a more uniform surface structure. The smaller particle size and closer contact

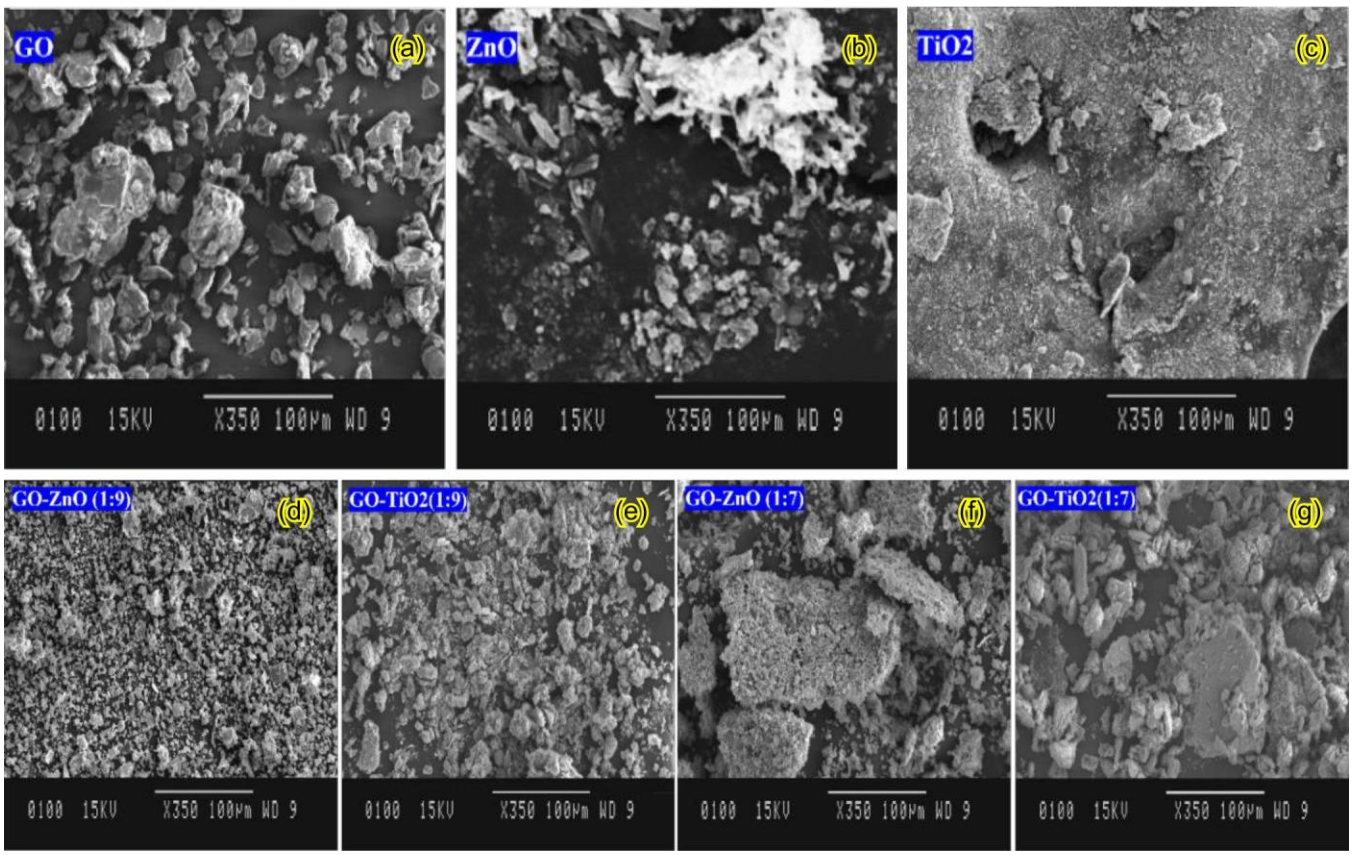


Fig. 3. SEM images of (a) GO, (b) ZnO and (c) TiO_2, (d) GO-ZnO (1:9), (e) GO-TiO_2 (1:9), (f) GO-ZnO (1:7) and (g) GO-TiO_2 (1:7)

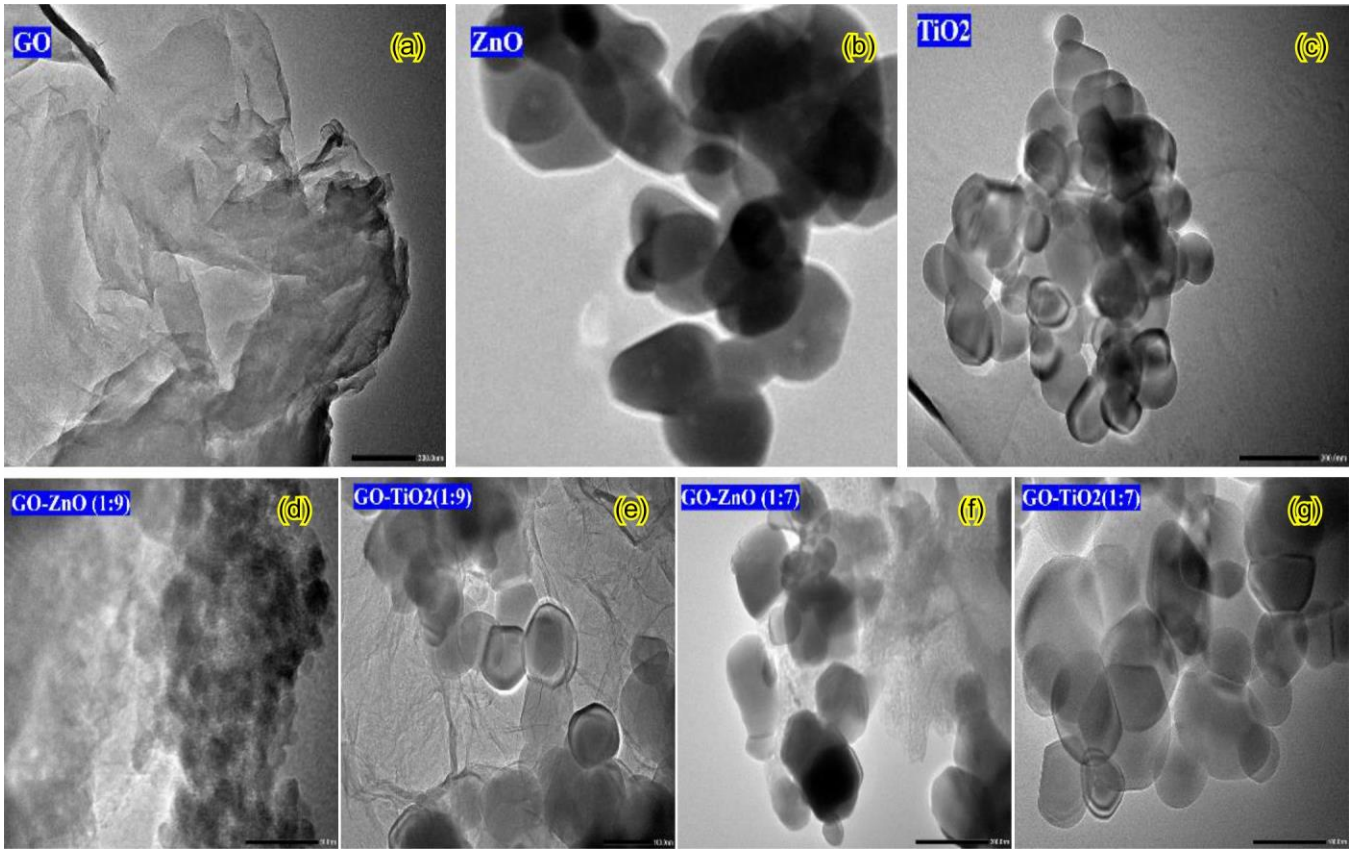


Fig. 4. HRTEM images of (a) GO, (b) ZnO and (c) TiO_2, (d) GO/ZnO (1:9), (e) GO/TiO_2 (1:9), (f) GO/ZnO (1:7) and (g) GO/TiO_2 (1:7)

between GO sheets and metal oxide nanoparticles may affect the surface properties and photocatalytic activity of the composites.

Photocatalytic activity: The photocatalytic activity of the synthesized samples was evaluated through the degradation of methylene blue (MB) and rose Bengal (RB) dyes (25 ppm) in aqueous solution under sunlight irradiation. The degradation process was monitored using a UV-Vis spectrophotometer by measuring the characteristic absorption maxima of MB (664 nm) and RB (550-555 nm).

Fig. 5a presents the photocatalytic performance of pristine ZnO under natural sunlight. The characteristic absorption peaks of methylene blue (MB) and Rose Bengal (RB) dyes decreased progressively during irradiation without noticeable wavelength shifts. ZnO achieved 96.4% MB degradation within 60 min and 99% RB degradation within 120 min. TiO_2 nanoparticles (Fig. 5b) showed a gradual decrease in the absorption intensity of both dyes. The degradation efficiencies reached 43.7% for MB and 37.2% for RB after 150 min. GO nanosheets (Fig. 5c) achieved 92.8% MB degradation and 96% RB degradation within 75 min. The results confirm the photocatalytic activity of all three materials under natural sunlight. ZnO exhibited the highest degradation efficiency among the pristine photocatalysts.

The GO/ZnO (1:9) nanocomposite (Fig. 6a) achieved 91% MB degradation within 50 min and 94% RB degradation within 60 min under natural sunlight. The decline in the absorbance during irradiation corresponds to a reduction in dye concentration. GO/TiO_2 (1:9) (Fig. 6b) showed 85% MB degradation within 90 min and 91% RB degradation within 70 min. The GO/ZnO (1:7) nanocomposite (Fig. 6c) exhibited faster degradation. It removed 94.4% of MB within 30 min and 97% of RB within 35 min. The rapid decline in the characteristic absorption peaks indicates faster dye removal by this composite. GO/TiO_2 (1:7) (Fig. 6d) achieved 90% MB degradation within 70 min and 93.5% RB degradation within 60 min. Its performance was higher than that of pristine TiO_2 under the tested conditions.

Before sunlight exposure, each photocatalyst-dye suspension was stirred in the dark for 30 min to establish adsorption–desorption equilibrium. The dark adsorption ranged from 0 to 8.1% for MB and 0 to 8.4% for RB depending on the photocatalyst. The dye concentration measured after this period was used as C_o for calculating the subsequent degradation efficiency. The reported sunlight-driven degradation values therefore exclude the initial dark adsorption step.

Control experiment (photolysis under sunlight): The control experiments were performed under natural sunlight without photocatalysts to assess the contribution of direct photolysis to MB and RB dyes removal. The UV-Vis spectra recorded at 0, 30 and 60 min showed only minor changes in the characteristic absorption peaks of both dyes. RB exhibitted approximately 8% self-degradation after 30 and 60 min (Fig. 7). These results indicate limited direct photolysis under the experimental conditions. The substantially higher dye removal observed in the presence of the synthesised nanocomposites can therefore be attributed mainly to photocatalytic activity.

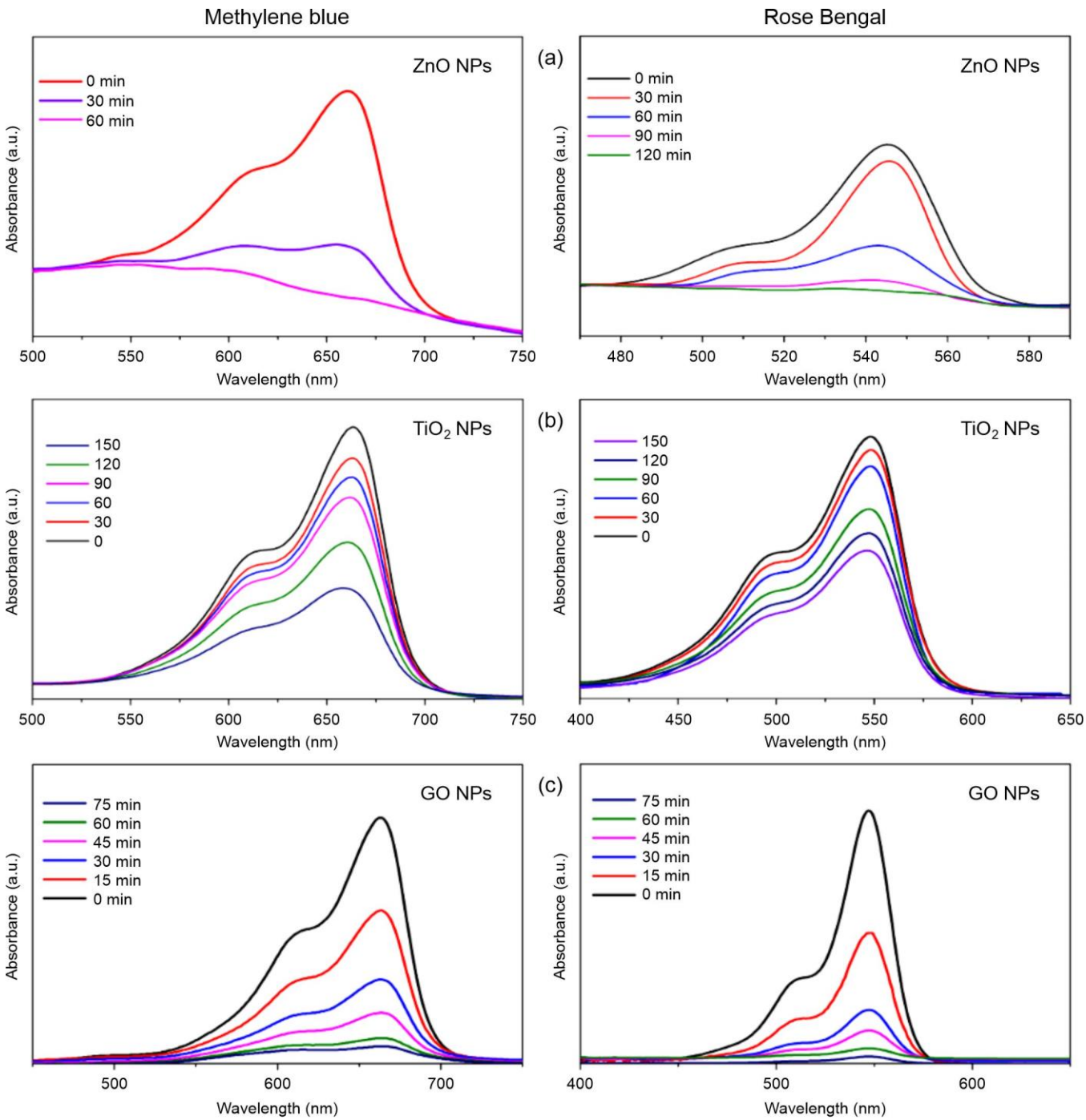


Fig. 5. Time-dependent UV–Vis spectra of methylene blue (left) and rose Bengal (right) degradation using GO-based photocatalysts

Comparative studies: Table-1 presents a comparison of the photocatalytic performance of representative GO/ZnO and GO/TiO_2 nanocomposites reported in previous studies. Degradation efficiencies of 91% to 99% have been reported for methylene blue and rose Bengal dyes using UV, visible light, solar or natural sunlight irradiation. For example, TiO_2/PPy/GO and ZnO/rGO composites showed 97-99% degradation of rose Bengal under visible-light within 120 min. GO-based ZnO nanorod systems also reported 97-98% degradation of methylene blue within 40-65 min. However, direct comparison of GO/ZnO and GO/TiO_2 photocatalysts is difficult since the reported studies use different catalyst composition, light sources, pollutants and experimental conditions.

Photocatalytic degradation and kinetic analysis: The dye removal experiments were conducted using GO, TiO_2, ZnO and their GO-based nanocomposites with methylene blue (MB) and rose Bengal (RB) dyes under natural sunlight. Before irradiation, the catalyst–dye suspensions were stirred in dark for 30 min to establish adsorption–desorption equilibrium. The dye concentration measured after this period was taken as C_o for kinetic analysis. The decrease in dye concentration during dark stirring was attributed to adsorption. The

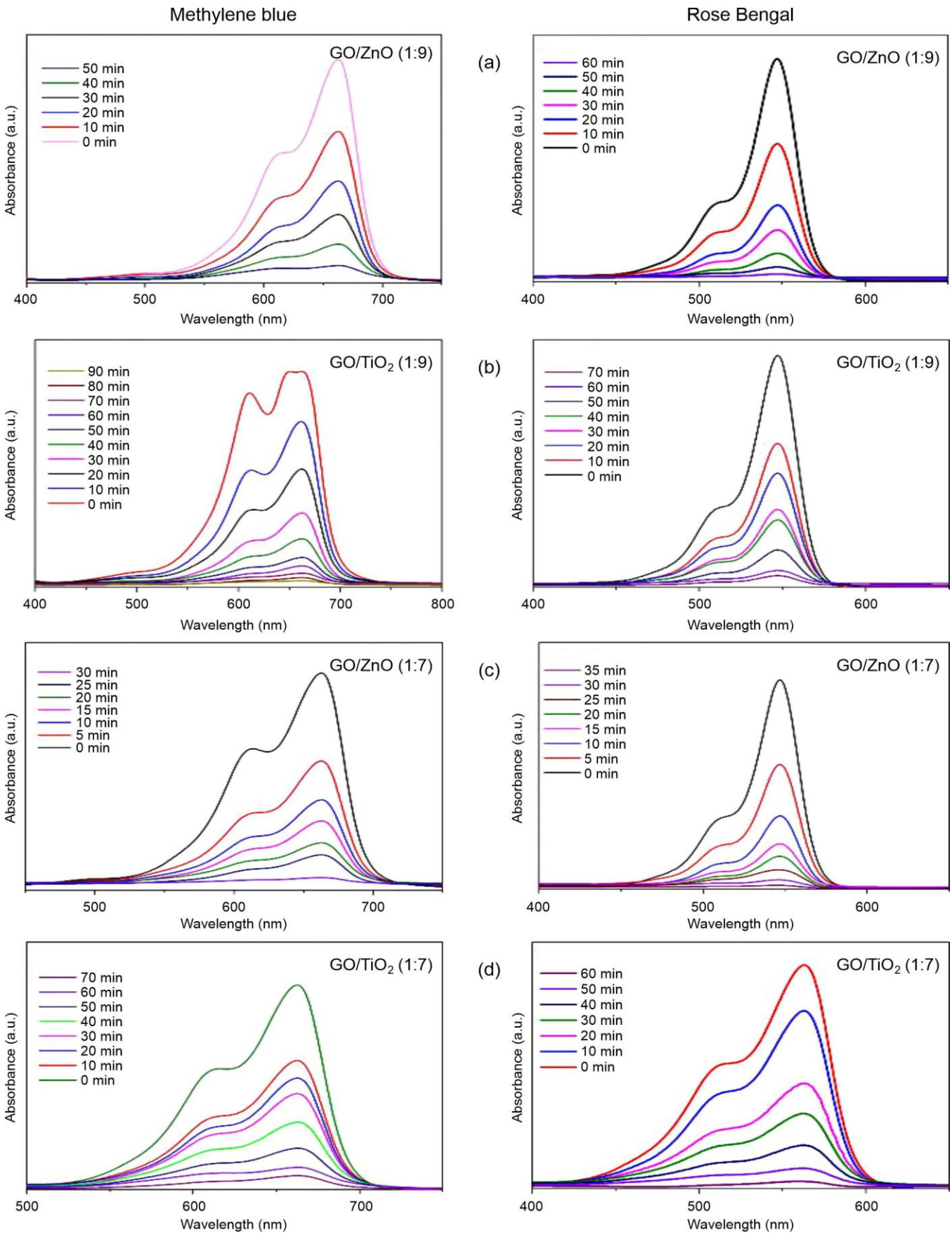


Fig. 6. Time-dependent UV–Vis spectra of methylene blue (MB) and rose Bengal (RB) dye (a) GO/ZnO (1:9), (b) GO/TiO_2 (1:9), (c) GO/ZnO (1:7) and (d) GO/TiO_2 (1:7) nanocomposites

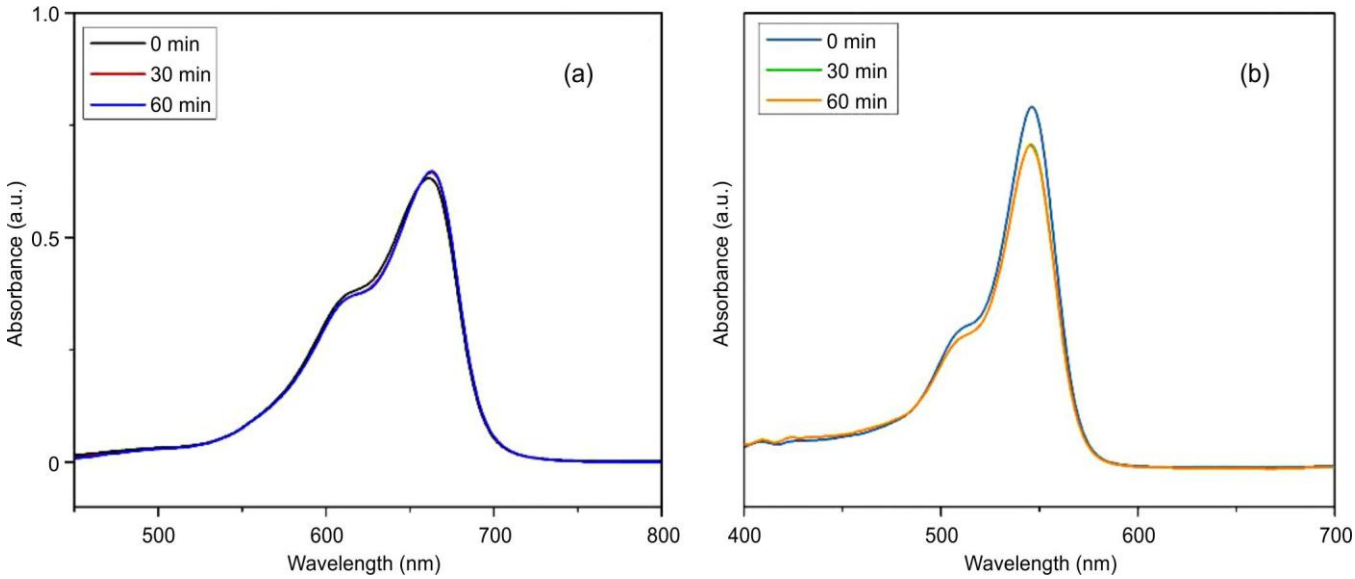


Fig. 7. UV-Vis spectra of MB and RB under natural sunlight without photocatalyst which show the negligible photolytic degradation

TABLE-1
COMPARISON OF REPORTED PHOTOCATALYTIC EFFICIENCIES OF GO COMPOSITES

Catalyst	Specific catalyst composition	Dye	Degradation efficiency (%)	Time (min)	Light source	Ref.
GO/ZnO	GOZ-10 (ZnO nanorods on 10% GO)	MB	98.0	65	Sunlight	[24]
ZnO/rGO	ZnO/rGO	RB	97-99	120	Visible light	[47]
GO/ZnO	Gr–ZnO (Radially grown nanorods)	MB	97.5	40	Solar irradiation	[48]
GO/TiO_2	GO/PANI/TiO_2 (Hybrid nanocomposite)	MB	98.9	60	UV light	[49]
GO/ZnO	ZnO/GO (Biomass mediated)	MB	91.0	80	Visible	[50]
GO/TiO_2	TiO_2/PPy/GO (Polypyrrole hybrid)	RB	97.0	120	Visible light	[51]

subsequent decrease during sunlight exposure was used to assess light-induced degradation. In this study, degradation refers to decolorization based on the decrease in absorbance at the characteristic wavelength of each dye.

The degradation profiles were evaluated using normalized concentration plots (C/C_o *versus* time). The reaction kinetics were examined using pseudo-first-order plots of $\ln(C_o/C)$ versus irradiation time (Fig. 8). All photocatalysts showed a gradual decrease in dye concentration with increasing irradiation time. GO exhibited relatively high dye removal. This behaviour may be related to its oxygen containing functional groups and their interactions with dye molecules. ZnO showed faster degradation kinetics than TiO_2 for both dyes, as indicated by its higher apparent rate constants and steeper kinetic slopes.

GO incorporation enhanced the degradation kinetics of both ZnO- and TiO_2-based composites compared with the corresponding pristine metal oxides. This improvement may arise from interactions between GO and the metal oxide phases. Changes in dye adsorption and nanoparticle distribution may also contribute to the observed behaviour. Among the investigated materials, GO/ZnO (1:7) exhibited the highest apparent rate constants for both MB and RB. Its rapid decrease in C/C_o and the steepest slopes in the kinetic plots indicate faster dye removal under the tested conditions. This performance may be related to the distribution of ZnO NPs across the GO sheets and interactions between the catalyst surface and dye molecules.

The degradation kinetics were described using a pseudo-first-order kinetics model expressed as:

$$\ln\left(\frac{C_o}{C}\right) = k_{app}t$$

where C_o, is the dye concentration measured after 30 min of dark stirring, immediately before the start of sunlight irradiation; C, is the dye concentration at irradiation time (t); and k_{app}, is the apparent reaction rate constant. A larger k_{app} corresponds to faster degradation kinetics.

The apparent rate constants reported in Table-2 were calculated from the initial linear region of the $\ln(C_o/C)$ *versus* irradiation time plots up to approximately 80% conversion. Linear regression was performed with the intercept fixed at zero. The same fitting range was applied to all photocatalysts to maintain consistency. Data points corresponding to the plateau region of the decolorization curves were excluded, as the pseudo-first-order model may no longer adequately describe the reaction in this region. Their inclusion would lower the fitted slope and underestimate the apparent rate constant. All apparent rate constants were verified against the degradation values reported in Table-3 using the pseudo-first-order equation: degradation (%) = $[1 - \exp(-k_{app}t)] \times 100$.

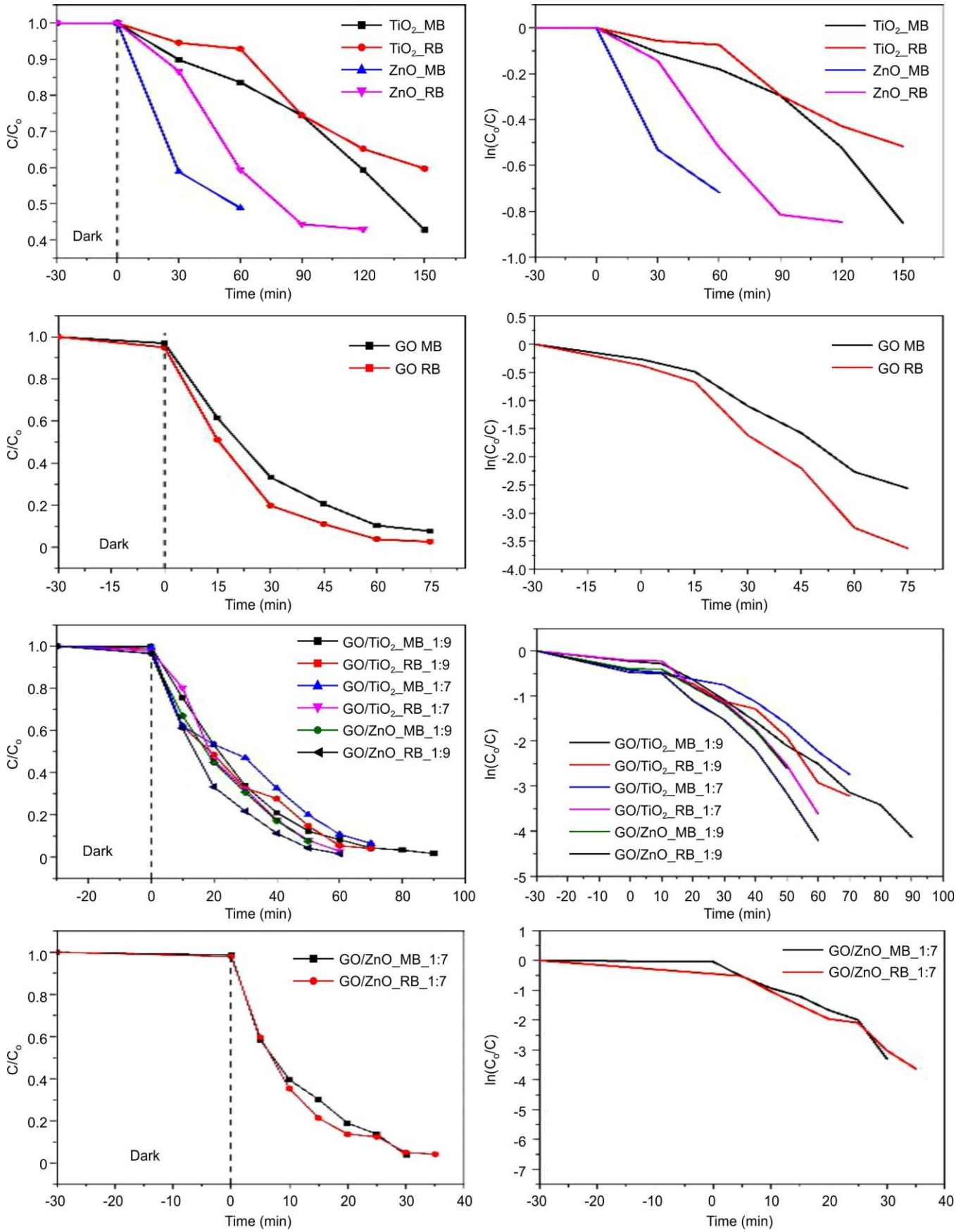


Fig. 8. Photocatalytic degradation efficiency and pseudo-first-order kinetic plot of TiO_2, ZnO, GO and GO-based nanocomposites under natural sunlight irradiation

TABLE-2
APPARENT PSEUDO-FIRST-ORDER RATE CONSTANTS (k_{app}, man^{-1}) AND REGRESSION COEFFICIENTS (R^2) FOR THE PHOTOCATALYTIC DEGRADATION OF METHYLENE BLUE (MB) AND ROSE BENGAL (RB)

Catalyst	MB k_{app} (min^{-1})	MB R^2	RB k_{app} (min^{-1})	RB R^2
ZnO	0.0110	0.85684	0.0070	0.92836
TiO_2	0.0038	0.94420	0.0031	0.87050
GO	0.0350	0.99174	0.0500	0.98728
GO/ZnO (1:9)	0.0490	0.96630	0.0670	0.96832
GO/TiO_2 (1:9)	0.0458	0.94891	0.0463	0.99256
GO/ZnO (1:7)	0.0960	0.92505	0.0980	0.97954
GO/TiO_2 (1:7)	0.0370	0.94660	0.0500	0.94538

Constants determined from the linear region of $\ln(C_o/C)$ *versus* irradiation time up to 80 % conversion, with the fit constrained through the origin; the same criterion was applied to every sample.

TABLE-3
COMPARATIVE DYE DEGRADATION EFFICIENCY OF PHOTOCATALYSTS BEFORE AND AFTER ADSORPTION

Photocatalyst	Methylene blue (MB)			Rose Bengal (RB)		
	Dark adsorption after 30 min (%)	Degradation (%)	Time (min)	Dark adsorption after 30 min (%)	Degradation (%)	Time (min)
ZnO	Less than 1	96.4	60	Less than 1	99.0	120
TiO_2	Less than 1	43.7	150	Less than 1	37.2	150
GO	5.0	92.8	75	5.7	96.0	75
GO/ZnO (1:9)	8.1	91.0	50	8.4	94.0	60
GO/TiO_2 (1:9)	6.2	85.0	90	6.7	91.0	70
GO/ZnO (1:7)	2.1	94.4	30	1.4	97.0	35
GO/TiO_2 (1:7)	4.3	90.0	70	6.0	93.5	60

The GO/ZnO (1:7) composite exhibited the highest apparent rate constant among the investigated materials, followed by GO/ZnO (1:9). The higher k_{app} values of the GO-based composites reflect faster degradation kinetics under the tested sunlight conditions. Rose Bengal generally showed faster degradation than methylene blue with most composites. This difference may arise from variations in molecular structure and adsorption affinity as well as interactions between the dyes and catalyst surfaces.

Under sunlight irradiation, photogenerated electrons and holes may participate in reactions with dissolved oxygen and water, leading to the formation of reactive species such as superoxide and hydroxyl radicals. These species may contribute to dye decolorization. The decrease in dye concentration during irradiation was consistent with the changes observed in the corresponding UV-Vis absorption spectra.

Conclusion

Graphene oxide (GO), GO/ZnO and GO/TiO_2 nanocomposites were successfully synthesized *via* a modified Hummers' method followed by hydrothermal treatment. XRD, FTIR, SEM and HRTEM analyses confirmed the formation of GO-supported metal oxide nanocomposites, with crystalline ZnO and TiO_2 nanoparticles distributed on the GO sheets. The GO-based nanocomposites exhibited faster sunlight-driven photocatalytic degradation kinetics than the corresponding pristine materials mainly in the case of TiO_2. Among the investigated photocatalysts, GO/ZnO (1:7) showed the fastest degradation, achieving 94.4% degradation of methylene blue within 30 min and 97% degradation of rose Bengal within 35 min, while GO/TiO_2 (1:7) attained 90% and 93.5% degradation, under the investigated conditions. Although bare ZnO showed high final degradation efficiency, GO/ZnO (1:7) showed faster degradation within a shorter irradiation time. The faster degradation kinetics may be associated with the combined effects of dye adsorption and interfacial interactions between GO and the metal oxide phases. The degradation kinetics were evaluated using a pseudo-first-order model, with the corresponding apparent rate constants compared among the investigated photocatalysts. Compared with previously reported GO-based photocatalysts requiring approximately 40-120 min to achieve >95% degradation, the GO/ZnO (1:7) achieved 97% rose Bengal degradation within 35 min under natural sunlight, which indicates faster degradation under the investigated conditions. These findings suggest that GO/ZnO (1:7) is a promising sunlight-responsive photocatalyst for dye degradation under the investigated conditions.

ACKNOWLEDGEMENTS

The authors thank Ishu, Research Scholar and Department of Chemical Engineering of Deenbandhu Chhotu Ram University of Science & Technology, Murthal (Haryana) for their support in this study.

CONFLICT OF INTEREST

The authors declare that there is no conflicts of interest regarding the publication of this article.

DECLARATION OF AI-ASSISTED TECHNOLOGIES

During the preparation of this manuscript, the authors used an AI-assisted tool(s) to improve the language and no data, results or scientific conclusions were generated by AI. All analyses, interpretations and conclusions are the authors' own. The authors reviewed and edited the content and take full responsibility for the published work.

REFERENCES

1. A.B. Isaev, N.S. Shabanov, A.G. Magomedova, P.V. Nidheesh and M.A. Oturan, *Environ. Chem. Lett.*, **21**, 2863 (2023); https://doi.org/10.1007/s10311-023-01610-5
2. R. Lal, *Agronomy J.*, **107**, 1526 (2015); https://doi.org/10.2134/agronj15.0045
3. R.P. Schwarzenbach, T. Egli, T.B. Hofstetter, U. Von Gunten and B. Wehrli, *Annu. Rev. Environ. Resour.*, **35**, 109 (2010); https://doi.org/10.1146/annurev-environ-100809-125342
4. F.A. Alharthi, A. Ali Alghamdi, H.S. Alanazi, A.A. Alsyahi and N. Ahmad, *Catalysts*, **10**, 1457 (2020); https://doi.org/10.3390/catal10121457
5. A. Bafana, S.S. Devi and T. Chakrabarti, *Environ. Rev.*, **19(NA)**, 350 (2011); https://doi.org/10.1139/a11-018
6. T. Chellapandi and G. Madhumitha, *Environ. Qual. Manage.*, **33**, 105 (2024); https://doi.org/10.1002/tqem.22021
7. G. Anandhi and M. Iyapparaja, *RSC Adv.*, **14**, 9003 (2024); https://doi.org/10.1039/D4RA00711E
8. S. Homaeigohar, *Nanomaterials*, **10**, 295 (2020); https://doi.org/10.3390/nano10020295
9. G. Heidari and F. Kordbacheh, *Mater. Chem. Horiz.*, **2**, 139 (2023); https://doi.org/10.22128/mch.2023.684.1039
10. S. Bhattacharyya, L. Donato, S. Chakraborty, V. Calabrò, M. Davoli and C. Algieri, *Earth Syst. Environ.*, **9**, 639 (2025); https://doi.org/10.1007/s41748-024-00527-5
11. W.S. Hummers Jr. and R.E. Offeman, *J. Am. Chem. Soc.*, **80**, 1339 (1958); https://doi.org/10.1021/ja01539a017
12. D.C. Marcano, D.V. Kosynkin, J.M. Berlin, A. Sinitskii, Z. Sun, A. Slesarev, L.B. Alemany, W. Lu and J.M. Tour, *ACS Nano*, **4**, 4806 (2010); https://doi.org/10.1021/nn1006368
13. M.S.A. Bhuyan, M.N. Uddin, M.M. Islam, F.A. Bipasha and S.S. Hossain, *Int. Nano Lett.*, **6**, 65 (2016); https://doi.org/10.1007/s40089-015-0176-1
14. S.N. Alam, N. Sharma and L. Kumar, *Graphene*, **6**, 1 (2017); https://doi.org/10.4236/graphene.2017.61001
15. A. Saravanan, P.S. Kumar, S. Srinivasan, S. Jeevanantham, M. Vishnu, K.V. Amith, R. Sruthi, R. Saravanan and D.-V.N. Vo, *Chemosphere*, **298**, 134284 (2022); https://doi.org/10.1016/j.chemosphere.2022.134284
16. J. Tripathy, A. Mishra, M. Pandey, R.R. Thakur, S. Chand, P.R. Rout and M.K. Shahid, *Water*, **16**, 1481 (2024); https://doi.org/10.3390/w16111481
17. L. Yu, W. Xu, H. Liu and Y. Bao, *Catalysts*, **12**, 1340 (2022); https://doi.org/10.3390/catal12111340
18. S. Mohan, M. Vellakkat, A. Aravind and U. Reka, *Nano Express*, **1**, 030028 (2020); https://doi.org/10.1088/2632-959X/abc813
19. G. Nagaraju, G.C. Shivaraju, G. Banuprakash and D. Rangappa, *Mater. Today Proc.*, **4**, 11700 (2017); https://doi.org/10.1016/j.matpr.2017.09.085
20. S.S. Muniandy, N.H. Mohd Kaus, Z.-T. Jiang, M. Altarawneh and H.L. Lee, *RSC Adv.*, **7**, 48083 (2017); https://doi.org/10.1039/C7RA08187A
21. K.S. Swathi and K.G. Naik, *Discov. Ind. Chem. Mater.*, **1**, 3 (2026); https://doi.org/10.1007/s44508-026-00003-0
22. R.M.N.M. Rathnayake, H.W.M.A.C. Wijayasinghe, H.M.T.G.A. Pitawala, M. Yoshimura and H.-H. Huang, *Appl. Surf. Sci.*, **393**, 309 (2017); https://doi.org/10.1016/j.apsusc.2016.10.008
23. J.H. Kim, G.H. Shim, T.T.N. Vo, B. Kweon, K.M. Kim and H.S. Ahn, *RSC Adv.*, **11**, 3645 (2021); https://doi.org/10.1039/D0RA10207E
24. A. Khan, A.A. Shah, S.O. Allehabi, F. Ahmed, A. Alsulami and A. Azam, *Sci. Rep.*, **14**, 30696 (2024); https://doi.org/10.1038/s41598-024-78636-4
25. A. Kumar, *Int. J. Res. Appl. Sci. Eng. Technol.*, **6**, 339 (2018); https://doi.org/10.22214/ijraset.2018.2049
26. V. Mututu, A.K. Sunitha, R. Thomas, M. Pandey and B. Manoj, *Int. J. Electrochem. Sci.*, **14**, 3752 (2019); https://doi.org/10.20964/2019.04.49
27. R.E. Adam, E. Chalangar, M. Pirhashemi, G. Pozina, X. Liu, J. Palisaitis, H. Pettersson, M. Willander and O. Nur, *RSC Adv.*, **9**, 30585 (2019); https://doi.org/10.1039/C9RA06273D
28. P. Chhattise, S. Saleh, V. Pandit, S. Arbuj and V. Chabukswar, *Mater. Adv.*, **1**, 2339 (2020); https://doi.org/10.1039/D0MA00403K
29. J. Li, Z. Jin, Y. Chao, A. Wang, D. Wang, S. Chen and Q. Qian, *Chemosensors*, **11**, 65 (2023); https://doi.org/10.3390/chemosensors11010065
30. D. Chen, F. Ma, B. Lei, W. Qiu, X. Jiang, H. Yu, H. Bi, Y. Yang and J. Shen, *RSC Adv.*, **7**, 41399 (2017); https://doi.org/10.1039/C7RA07801C
31. V. Štengl, S. Bakardjieva, T.M. Grygar, J. Bludská and M. Kormunda, *Chem. Cent. J.*, **7**, 41 (2013); https://doi.org/10.1186/1752-153X-7-41
32. H. Zhang, X. Wang, N. Li, J. Xia, Q. Meng, J. Ding and J. Lu, *RSC Adv.*, **8**, 34241 (2018); https://doi.org/10.1039/C8RA06681G
33. S.S. Kumar, P. Venkateswarlu, V.R. Rao and G.N. Rao, *Int. Nano Lett.*, **3**, 30 (2013); https://doi.org/10.1186/2228-5326-3-30
34. S. Mugundan, B. Rajamannan, G. Viruthagiri, N. Shanmugam, R. Gobi and P. Praveen, *Appl. Nanosci.*, **5**, 449 (2015); https://doi.org/10.1007/s13204-014-0337-y
35. B. Bulcha, J. Leta Tesfaye, R. Shanmugam, L.P. Dwarampudi, N. Nagaprasad, V.L.N. Bhargavi, D. Anatol, and R. Krishnaraj, *J. Nanomater.*, **2021**, 1 (2021); https://doi.org/10.1155/2021/8617290
36. M. Handayani, E. Sulistiyono, F. Rokhmanto, N. Darsono, P.L. Fransisca, A. Erryani and J.T. Wardono, *IOP Conf. Ser.: Mater. Sci. Eng.*, **578**, 012073 (2019); https://doi.org/10.1088/1757-899X/578/1/012073
37. D. Khalili, *New J. Chem.*, **40**, 2547 (2016); https://doi.org/10.1039/C5NJ02314A
38. G. Surekha, K.V. Krishnaiah, N. Ravi and R. Padma Suvarna, *J. Phys. Conf. Ser.*, **1495**, 012012 (2020); https://doi.org/10.1088/1742-6596/1495/1/012012
39. I. Zarafu, I. Mușat, C. Limban, D.C. Nuță, I.D. Dulama, C. Radulescu, R.M. Stirbescu, A. Tatibouet, C.M. Chifiriuc, L. Marutescu, M. Popa, L.D. Dragu, E. Radu, I. Nicolau, C. Bleotu and P. Ionita, *Molecules*, **30**, 2585 (2025); https://doi.org/10.3390/molecules30122585
40. J. Liu, S. Chen, Y. Liu and B. Zhao, *J. Saudi Chem. Soc.*, **26**, 101560 (2022); https://doi.org/10.1016/j.jscs.2022.101560
41. S.S. An, K.-S. Yun and L. Zhong, *Int. J. Nanomedicine*, **2015**, 79 (2015); https://doi.org/10.2147/IJN.S88319
42. A. Hassen, E.A. Moawed, R. Bahy, A.B. El Basaty, S. El-Sayed, A.I. Ali and A. Tayel, *Sci. Rep.*, **14**, 22942 (2024); https://doi.org/10.1038/s41598-024-73007-5
43. P. Zhang, Y. Wang, D. Zhang, C. Liu, D. Wang, S. He, G. Hu and X. Tang, *RSC Adv.*, **6**, 91910 (2016); https://doi.org/10.1039/C6RA19674H
44. U. Diebold, *Surf. Sci. Rep.*, **48**, 53 (2003); https://doi.org/10.1016/S0167-5729(02)00100-0
45. J. Zhang, H. Yang, X. Xu, Y. Liu, H. Ren, P. Chen and K. Yang, *Phys. Status Solidi A Appl. Mater. Sci.*, **217**, 2000085 (2020); https://doi.org/10.1002/pssa.202000085
46. Y. Huang, R. Li, D. Chen, X. Hu, P. Chen, Z. Chen and D. Li, *Catalysts*, **8**, 151 (2018); https://doi.org/10.3390/catal8040151
47. B. Bhattacharyya, M. Geetha, H. Anwar, S.A. Zaidi, K.K. Sadasivuni, M. Mohamed, H. Sheikh, S.M. Alfarwati and R.A. Jarrar, *Int. J. Environ. Res.*, **19**, 34 (2025); https://doi.org/10.1007/s41742-024-00694-3
48. L. Khamkhash, A. Bazenova, K. Rustembekkyzy, B.Y. Balarabe and T.Sh. Atabaev, *Mater. Adv.*, **6**, 9495 (2025); https://doi.org/10.1039/D5MA00612K
49. S. Baruah, S. Kumar, B. Nayak and A. Puzari, *Polym. Bull.*, **78**, 1703 (2021); https://doi.org/10.1007/s00289-020-03182-8
50. S.A. Al-Zahrani, K. Umar, S.A. Tweib, J.A.M. Rashd, S.K. Afridi, S.A. Bhawani, A.A. Otaibi, N. Masood, D. Mansour, A. Khan and M. Ayyar, *Catalysts*, **13**, 409 (2023); https://doi.org/10.3390/catal13020409
51. A. Kumar and G. Pandey, *Desalination Water Treat.*, **114**, 265 (2018); https://doi.org/10.5004/dwt.2018.22312